Ceramics International 46 (2020) 8971–8978

Contents lists available at ScienceDirect

Ceramics International

journal homepage: www.elsevier.com/locate/ceramint

Photoluminescence and unique magnetoluminescence of transparent $(Tb_{1-x}Y_x)_3Al_5O_{12}$ ceramics

Zhifeng Xing, Mengmeng Lun, Wanying Wu, Hanzhao Song, Aihua Yao, Xunsheng Zhou, Yinzhen Wang*, Benli Chu, Wei Li, Qinyu He, Guannan He

Guangdong Engineering Technology Research Center of Efficient Green Energy and Environmental Protection Materials, Guangdong Key Laboratory of Quantum Engineering and Quantum Materials, School of Physics & Telecommunication Engineering, South China Normal University, Guangzhou, 510275, China

ARTICLE INFO

Keywords:
$(Tb_{1-x}Y_x)_3Al_5O_{12}$
Optical properties
Magnetic properties

ABSTRACT

Luminescent transparent ceramics $(Tb_{1-x}Y_x)_3Al_5O_{12}$ (x = 0, 0.2, 0.5, 0.8) are successfully prepared by a solid-state method with additional hot isostatic pressing (HIP) treatment, and the structure and properties are investigated by XRD, SEM, PL, UV–Vis spectrophotometry and ellipsometry. The Y-containing samples are shown to be solid solution phases between TAG and YAG. The PL intensity is 14 times stronger with the incorporation of 80 mol.% Y, and the $^5D_4 \rightarrow {}^7F_5$ emission lifetime of Tb^{3+} is prolonged from 0.357 to 3.035 ms at room temperature. A unique magnetoluminescence emerges upon the incorporation of Y, showing an interesting emission decrease to 55% as the Y content reaches 80 mol.%. Remarkably, this magnetoluminesence can occur at room temperature without an intense magnetic field. Based on our work, transparent $(Tb_{1-x}Y_x)_3Al_5O_{12}$ ceramics exhibit the potential for applications in green emitters, optical instruments and photoelectric devices. In particular, the magnetoluminescence provides a simple, noncontact and nondestructive route for probing magnetic fields.

1. Introduction

As a component of the RGB color system, the green emitter plays a fundamental role in multiphosphor-based white-LED illumination, displays, lasers, decorative lighting and optical instruments [1–5]. In recent years, researchers have discovered multiple green emitters comprising single crystals, phosphor powders, polycrystalline ceramics, glass, etc., such as $SrHfS_3$, $MgAlON:Mn^{2+}$, $[Ph_4P]_2[MnBr_4]$, $CsPbBr_3$, $CH_3NH_3PbBr_3$ and Tb^{3+}-doped $ZnO\text{-}B_2O_3\text{-}SiO_2$ [3,4,6–9]. These efforts have mainly been devoted to advances in simplicity, functionality, reliability, efficiency and luminous tunability.

Among all the categories of luminescent materials, inorganic transparent ceramics possess a much higher chemical stability and wear resistance than organic bases, a low-cost synthesis relative to single crystals, and extra optical features compared with phosphor powder, making them promising for photoelectric applications. Terbium aluminum garnet ($Tb_3Al_5O_{12}$, abbreviated as TAG), has been widely reported for its potential applications as Faraday isolators [10,11], and current research primarily focuses on advances in the ceramic transparency and magneto-optical properties [11–16]. However, less attention has been paid to the optimization of the TAG luminescence, which also deserves further exploration. TAG phosphor powder and single crystals have been prepared since early times, and a few attempts have proceeded for the modification of the luminescence [17–20]. In 2011, a transparent TAG ceramic was first reported, but little work has been devoted to the refinement of its luminescence properties. Actually, the green emission of Tb^{3+} that occurs in TAG is quite stable due to the nature of electron energy levels compared with that of other efficient luminescent centers. By taking advantage of that, it is probably that the luminescence intensity and lifetime can be improved by introducing other components with an easily controlled synthesis route. It is also highly meaningful to investigate the effect of a magnetic field on the luminescence of TAG-based transparent ceramics, which has hardly been reported in the current papers. Magnetoluminescence (ML) has been drawing more and more interest due to the attractive potential of novel magneto-optical dual-function materials, and the quest for the underlying physical mechanism is growing [21–23]. In applications, the magnetism-responsive character provides an alternative way of realizing tunable luminescence, data storage, and bioimaging [24–28] and suggests a simple, noncontact and nondestructive route for the detection of magnetic fields [29], which remains a challenge in some practical situations. Therefore, the study of the ML of TAG-based materials

* Corresponding author. School of Physics & Telecommunication Engineering, South China Normal University, No. 378, Waihuan West Rd., Panyu District, Guangzhou, China.
E-mail address: agwyz@aliyun.com (Y. Wang).

https://doi.org/10.1016/j.ceramint.2019.12.144
Received 18 October 2019; Received in revised form 11 December 2019; Accepted 14 December 2019
Available online 17 December 2019

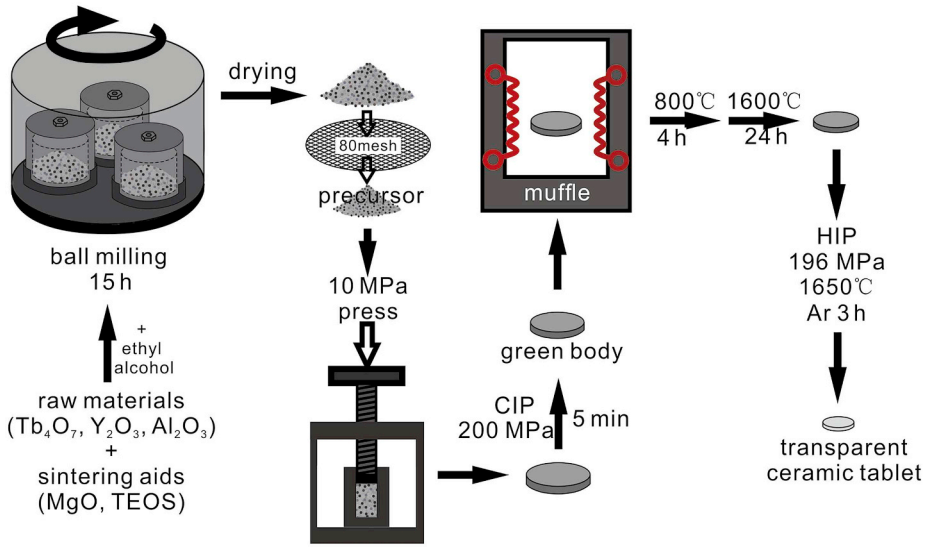

Fig. 1. The process for synthesizing transparent $(Tb_{1-x}Y_x)_3Al_5O_{12}$ (x = 0, 0.2, 0.5, 0.8) ceramic tablets.

has an essential significance in the development of new types of photoelectronic and magnetic devices.

In this paper, we have prepared luminescent transparent $(Tb_{1-x}Y_x)_3Al_5O_{12}$ (x = 0, 0.2, 0.5, 0.8) ceramics through a solid-state reaction and HIP posttreatment, and the crystal structure, microscopic morphology and optical properties of the samples were investigated.

2. Experimental method

The method for the preparation of all samples in this paper is based on the reported literature and our previous work [30,31]. The process for sample preparation is presented in Fig. 1. All chemical reagents needed were purchased from Aladdin Inc., CN. Tb_4O_7 (99.99%), Y_2O_3 (99.99%), and Al_2O_3 (99.99%) raw powders are weighed according to the exact stoichiometric ratios of $(Tb_{1-x}Y_x)_3Al_5O_{12}$ (x = 0, 0.2, 0.5, 0.8) and then fed into a ball mill along with 0.4 wt% TEOS (99.99%) and 0.08 wt% MgO (99.99%) as sintering aids. Afterwards, ethyl alcohol (99.99%) is added to the mixture for dispersion before the following 15 h ball milling process. Then, the obtained slurries are thoroughly dried in the oven, followed by an 80 mesh sieving to acquire homogeneous powder mixtures. A tablet machine is utilized to uniaxially press the powders into a Φ16 mm stainless steel mold under 10 MPa, and then the obtained tablets are cold isostatically pressed (CIP) for 5 min at 200 MPa to become the green bodies. A 4 h calcination of the tablets at 800 ℃ follows to remove the residual organics, and then a sintering process proceeds in a muffle for 24 h at 1600 ℃. Eventually, the tablets are treated by hot isostatic pressing (HIP) for 3 h under a 196 MPa Ar atmosphere. After the preparation, the ceramic tablets are polished on each side to 1.5 mm thick.

The crystal structures of the samples are identified by X-ray diffraction with a Bruker D8 Advance powder diffractometer (Cu K_α radiation, Germany). The microscopic observations of the samples are accomplished by SEM (JSM-6510, JEOL, Kariya, Japan). Steady-state PL and excitation spectra at room temperature are measured by a fluorescence spectrophotometer (FL-4500, Hitachi, Japan; Xe lamp as the light source) with a scan speed of 240 nm/min. The absorbance and in-line transmittance spectra are obtained with a UV–Vis spectrophotometer (UV-2600, Shimadzu, Japan). Luminescence lifetime and time-resolved emission decay measurements are performed by a fluorescence spectrometer (FLS980, Edinburgh Instruments, UK) with a 365 nm pulsed laser source. The refractive index curves are obtained through fitting the ellipsometric data collected at an angle of 64.53° using a Mueller matrix ellipsometer (ME-L ellipsometer, Wuhan Eoptics Technology Co., China). The magnetoluminescence behaviors are recorded by detecting the emission of samples laid on a few pieces of NdFeB ring magnets by a spectrophotometer (QE65 Pro, Ocean Optics Inc., China) with a 365 nm LED as the excitation light source. The intensity of the applied magnetic field is determined by a magnetometer.

3. Results and discussion

HIP, as a commonly used posttreatment method, proves to be effective for the expelling of poles between grain boundaries, which is crucial for the optical homogeneity and transparency. To determine the optimal sintering temperature, the relative densities of pure TAG ceramic are obtained after HIP treatment at different temperatures, as shown in Fig. 2, in which the highest relative density is attained at 1650 ℃. Generally, a higher relative density leads to superior optical properties. Thus, 1650 ℃ is considered to be the optimal HIP temperature for the preparation of Y-containing TAG ceramics.

3.1. Structure and morphology

Crystallographically, TAG belongs to a cubic crystal system with the symmetry O_h^{10}-Ia3d, each unit cell containing 8 chemical formula units [32]. The atomic stacking of TAG is commonly seen as a model featuring linkages between the coordination polyhedrons of $[TbO_8]$ dodecahedrons, $[AlO_6]$ octahedrons and $[AlO_4]$ tetrahedrons. Tb^{3+} is

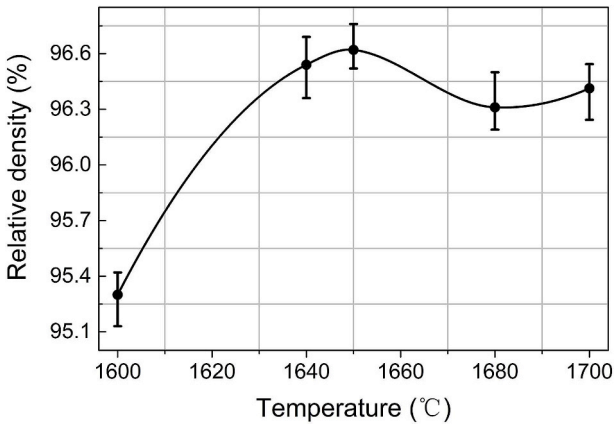

Fig. 2. Relative density of pure TAG ceramics (x = 0) as a function of the HIP temperature (The error bars have been shown).

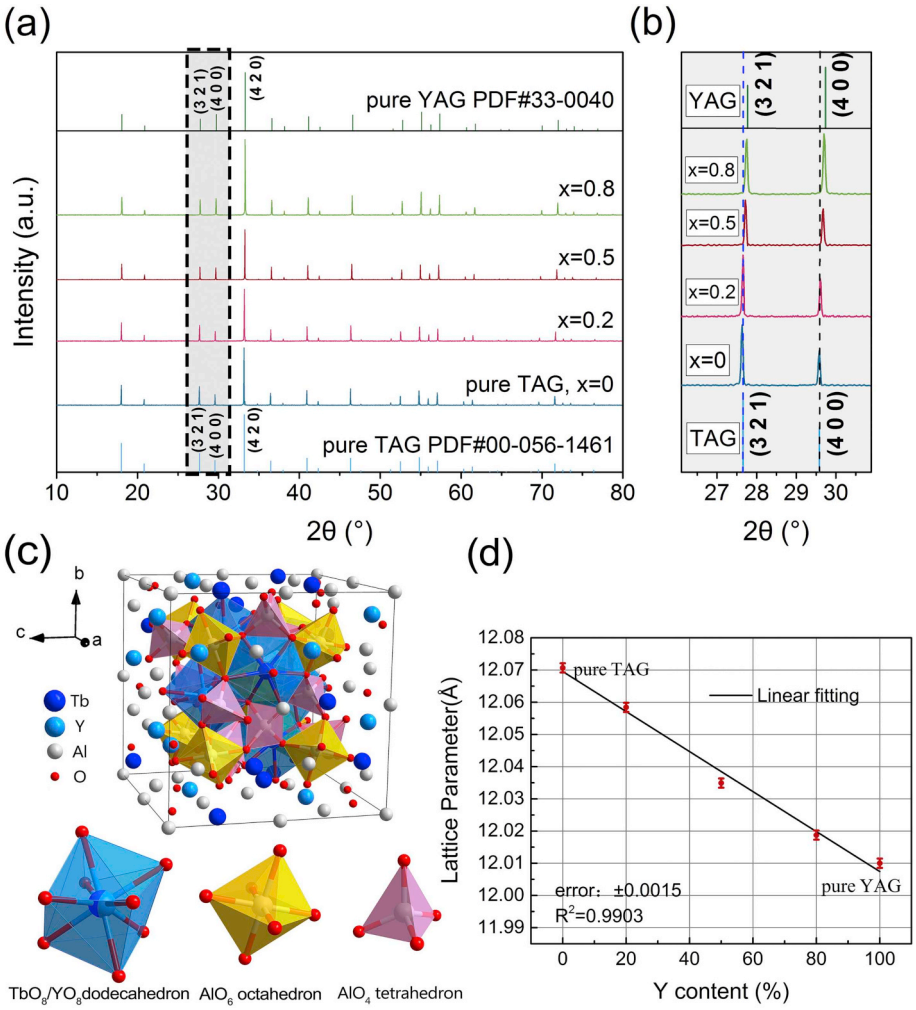

Fig. 3. (a) XRD patterns of the 1650 ℃ HIPed $(Tb_{1-x}Y_x)_3Al_5O_{12}$ ceramic tablets. (b) Enlargements of the XRD patterns from 26° to 31°. (c) Structure of the crystal lattice of $(Tb_{0.5}Y_{0.5})_3Al_5O_{12}$ plus the coordination polyhedron models of the metal ions. (d) Calculated lattice parameter and linear fitting curve as a function of the Y content (The error for the experimental data and R^2 value standing for the quality of the fitting are listed).

surrounded by 8 oxygen ions to form a distorted dodecahedron, and all the Tb^{3+} sites in a unit cell are equivalent despite the local orientation differences [32].

Fig. 3a displays the XRD patterns of the 1650 ℃ HIPed $(Tb_{1-x}Y_x)_3Al_5O_{12}$ ceramic tablets as well as the standard PDF patterns of YAG (yttrium aluminum oxide, $Y_3Al_5O_{12}$, PDF#33–0040) and TAG (PDF#00-056-1461). For the pure TAG sample (x = 0), the peaks match up pretty consistently with those of the standard TAG pattern, with the intensity of the (321) peak higher than that of the (400) peak. The Y-containing set of patterns is quite analogous without any peaks of impurity, and all peaks appear to be rather sharp with good symmetry. However, we have spotted slight position shifts and relative intensity variations of particular peaks. In Fig. 3b, as the Y amount increases, the peaks gradually shift towards larger angles along with the inversion of the relative intensity. When x = 0.8, the peak positions appear to be pretty close to those of pure YAG, and the (400) peak gets higher than the (321) peak, which is also consistent with pure YAG. Similar changes occur for other peaks.

In principle, Y^{3+} is able to replace Tb^{3+} in the lattice as a result of the similarity of their ionic radii (Tb^{3+}: 1.04 Å, Y^{3+}: 1.019 Å, for 8 coordination; Al^{3+}: 0.39 Å and 0.535 Å for 4 and 6 coordination, respectively) and ionic charges. The evolution of the XRD patterns can be attributed to the lattice shrinkage caused by the substitution of the smaller Y^{3+} for Tb^{3+}. Additionally, it is clear that the diminution of the d-spacing between crystal planes results in a right shift of the diffraction peak, according to Bragg's law. Fig. 3c provides the structure of the $(Tb_{0.5}Y_{0.5})_3Al_5O_{12}$ crystal lattice and the polyhedron models, showing the placement and connection types of the coordination polyhedrons. Due to the equivalence of all Tb^{3+} sites, the substitution of Y^{3+} should be uniform and coherent. Theories of the solid solution reveal that if (1) the ionic radius difference Δ ($\Delta = (r_1 - r_2)/r_1$) of the substituting ion and original ion is less than 15% (in this case, 2.0%), (2) the valence states of the ions are the same, and (3) the crystal structures of the two pure phases are identical, it is possible to form a continuous solid solution. In our case, these conditions are completely satisfied. Additionally, TAG and YAG have rather close lattice sizes (a = 12.074, 12.01 Å, respectively) and the same garnet structure [33]. Hence, it is reasonable to assume that by introducing Y, the sample gradually transforms from TAG (x = 0) into solid solution phases $(Tb_{1-x}Y_x)_3Al_5O_{12}$, alongside slight changes in the lattice size.

We have also calculated the lattice parameters from the XRD data, as presented in Fig. 3d. A linear relation between the lattice parameter and Y concentration is demonstrated by the fitting line to attest to the solid solution phases [34], according to Vegard's law (see Eq. (1)), a well-known empirical rule for solid solutions:

$$a_{AB} = c_A a_A + (1 - c_A) a_B \quad (1)$$

where a_{AB}, a_A, and a_B represent the lattice parameters of the A-B solid solution, A and B, respectively, and c_A is the concentration of A. In general, we have successfully prepared samples of the designed

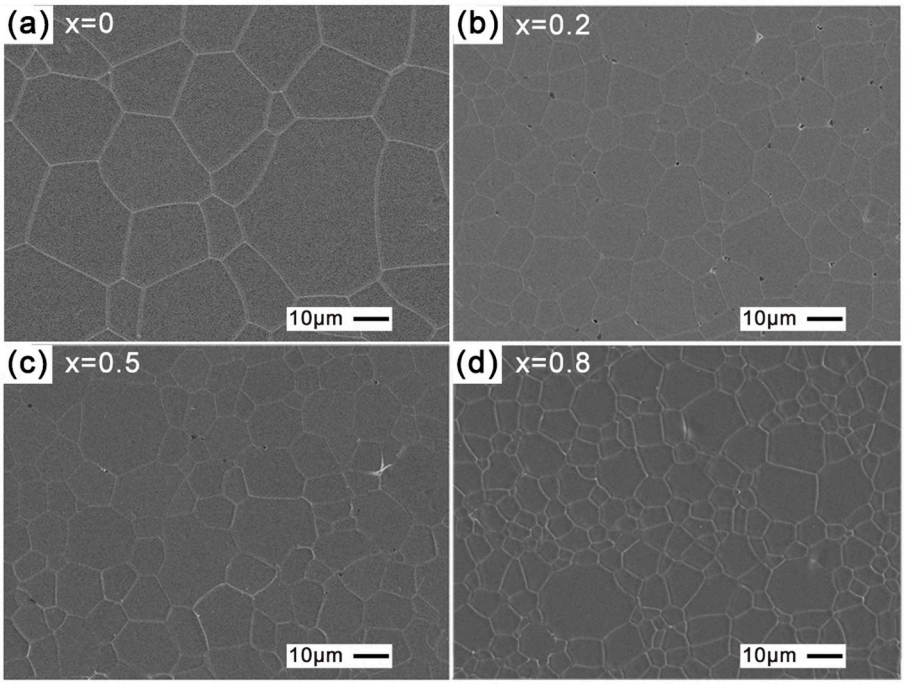

Fig. 4. SEM images of the 1450 ℃ thermal-etched surfaces of the samples. (a) pure TAG, (b) $(Tb_{0.8}Y_{0.2})_3Al_5O_{12}$, (c) $(Tb_{0.5}Y_{0.5})_3Al_5O_{12}$, (d) $(Tb_{0.2}Y_{0.8})_3Al_5O_{12}$.

compositions without any detectable secondary phase, which is highly essential for realizing transparency, isotropy and other optical properties.

The surface SEM morphology of the thermal-etched samples is presented in Fig. 4. It is noted that all samples exhibit relatively uniform grains without abnormal growth and clean grain boundaries. Only a couple of poles can be seen in the images, indicating a fairly good densification of the ceramics, which is of great benefit to the optical quality. As the Y content increases, the average grain size declines while the grain boundaries increase, probably because the introduction of Y suppresses grain growth.

3.2. Absorbance, transmittance and refractive index

The absorbance spectra of the transparent $(Tb_{1-x}Y_x)_3Al_5O_{12}$ ceramics in the UV–vis region are presented in Fig. 5a. The peaks at 485, 377, and 352 nm are attributed to the 4f-4f transitions of Tb^{3+} from $^7F_6$ to $^5D_4$, $^5D_3$ and $^5D_2$, respectively. The 325 nm peak is due to the spin-forbidden (E_1) transition of Tb^{3+} [20]. No absorption peak of Tb^{4+} can be found in the spectra [17]. All the absorption peaks largely maintain consistency for samples with different Y contents, which means that the addition of Y does not introduce new absorption to the TAG samples in the studied region. However, a significant decline in the absorption is noted when the concentration of Y^{3+} increases, as a result of the decrease in the overall absorption of Tb^{3+}. The in-line transmittance spectra of the samples are shown in Fig. 5b. Absorption peaks emerge at 485 and 376 nm, in accord with the absorbance spectra. The transmittance of the pure TAG ceramic rises along with the increase in the wavelength but only reaches approximately 50% at 700 nm. By contrast, the transmittances of the $(Tb_{0.5}Y_{0.5})_3Al_5O_{12}$ and $(Tb_{0.8}Y_{0.2})_3Al_5O_{12}$ ceramics exceed 50% in the region of 400–1100 nm, and that of the $(Tb_{0.2}Y_{0.8})_3Al_5O_{12}$ ceramic generally reaches 65%. This result reveals that the transmittance of the TAG ceramic can apparently be enhanced by increasing the amount of Y doping, and this is beneficial in optical applications.

Fig. 6 shows the fitted refractive index curves of samples based on ellipsometric data. The curves of the solid solution samples are plotted by fitting the ellipsometric data. Curves of pure YAG and TAG are

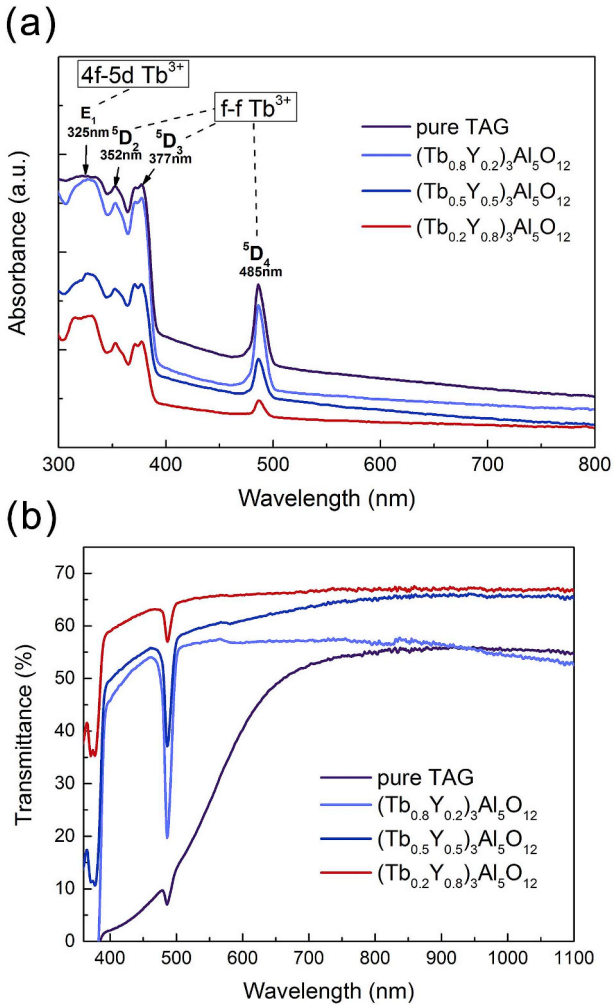

Fig. 5. (a) UV–vis and (b) in-line transmittance spectra of $(Tb_{1-x}Y_x)_3Al_5O_{12}$ ceramics.

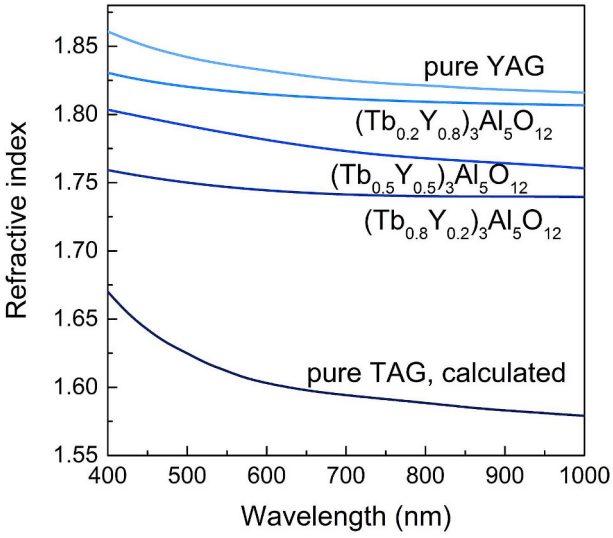

Fig. 6. Refractive index curves.

obtained from the literature [35,36]. It can be noted that all curves decrease monotonically in the vis-NIR region, which is a general rule for transparent materials. Apparently, the refractive index increases as the amount of Y rises, and the curve gradually evolves from TAG to YAG. This can be considered the transformation of the optical properties from those of TAG to those of YAG through intermediate phases of $(Tb_{1-x}Y_x)_3Al_5O_{12}$ (x = 0.2, 0.5, 0.8) [37], on account of the similarity in the crystal structure and the homogeneous atomic substitution.

3.3. Photoluminescence

Fig. 7a shows the excitation and photoluminescence (PL) spectra of $(Tb_{1-x}Y_x)_3Al_5O_{12}$ ceramics with different Y contents under detected wavelengths of 543 and 325 nm, respectively. Excitation spectra ranging from 350 to 400 nm are ascribed to f-f transitions of Tb^{3+}, and the peaks within the range from 280 to 350 nm are attributed to 4f-5d transitions of Tb^{3+}. Strong emission peaks at 493, 543, 587, and 624 nm and weak peaks in the range of 670–710 nm are detected, corresponding to the $^5D_4 \rightarrow {}^7F_J$ (J = 6, 5, 4, 3, 2, 1, 0) transitions of Tb^{3+} [36], as also shown by the schematic diagram in Fig. 7b [38–40]. The overall integrated PL intensities are calculated in the inset of Fig. 2a. Apparently, the luminescence intensifies as the Y content increases due to the diminution of nonradiative centers, which coincides well with other literature [41]. Fig. 7c shows the CIE-1931 color space chromaticity diagram, indicating a slight shift of the color coordinates as the concentration of Y increases, mainly as a result of the relatively weakened $^5D_4 \rightarrow {}^7F_{2,1,0}$ peaks. The inset of Fig. 7c shows a typical strong green emission of the sample under the excitation of a 365 nm LED source, proving our samples to be highly efficient luminescent ceramics.

Fig. 8a shows the decay curves of the Tb^{3+} $^5D_4 \rightarrow {}^7F_5$ emission for $(Tb_{1-x}Y_x)_3Al_5O_{12}$ ceramics under 365 nm pulsed excitation. A single exponential fitting model with the form of Eq. (2) is applied to all curves:

$$I(t) = A \exp\left(-\frac{t}{\tau}\right) \tag{2}$$

The lifetime τ of all the samples is calculated from the fitting, and the results are presented in Fig. 8a. It shows that as the amount of Y rises, the lifetime of the Tb^{3+} $^5D_4 \rightarrow {}^7F_5$ emission increases from 0.357 to 3.035 ms as a result of the attenuated interactions between the luminescent and quenching centers, thus significantly improving the stability of the $^5D_4$ energy level of Tb^{3+}. Moreover, the increased emission in Fig. 7a can be further illustrated by the enhancement of the lifetime, according to Eq. (3) [42].

$$I_{ss} = \int_0^\infty I_0 \exp\left(-\frac{t}{\tau}\right) dt = I_0 \tau \tag{3}$$

It can be noted that I_{ss} is proportional to τ if I_0 is kept a constant, where I_{ss} represents the emission intensity, τ represents the emission lifetime, and I_0 can be considered as a parameter that depends on the fluorophore concentration and a number of instrumental parameters.

In Fig. 8a, we find that the fittings of the curves with x = 0.5 and 0.8 coincide well, while the other two fittings deviate obviously from the experimental curves, which can be clearly seen from the inset of Fig. 8a. This phenomenon has also been found in $Y_{1-x}Tb_xBO_3$ material with a high concentration of Tb^{3+} [43]. The deviation from the fitting is caused by a radiationless process involving Tb^{3+} ions and impurities. To further explore the exact interaction mechanism of Tb^{3+}, here, we assume the interaction to be of a multipolar type; thus, the decay behaviors of $(Tb_{0.8}Y_{0.2})_3Al_5O_{12}$ and pure TAG samples are analyzed by the direct quenching scheme [32,43], according to the well-known Inokuti and Hirayama's model referred to in Eq. (4):

$$\frac{I(t)}{I_0} = \exp\left[-\frac{t}{\tau} - k(t)\right] \tag{4}$$

where τ represents the intrinsic lifetime for a single ion and k(t) is described by Eq. (5) according to the Förster resonance energy transfer (FRET) mechanism:

$$k(t) = \left(\frac{C}{C_0}\right)\left(\frac{t}{\tau}\right)^{\frac{3}{S}} \Gamma\left(1 - \frac{3}{S}\right) \tag{5}$$

where the S value stands for dipole-dipole, dipole-quadrupole, and quadrupole-quadrupole interactions. C_0 and γ are constants, and C represents the number of acceptors in a unit volume [40,44].

In Fig. 8b, the experimental data from the time-resolved emission measurement of the $^5D_4 \rightarrow {}^7F_5$ transition of Tb^{3+} is plotted to be analyzed through Inokuti and Hirayama's model, according to Eq. (6).

$$\ln\left[-\ln\left(\frac{I(t)}{I_0}\right) - \left(\frac{t}{\tau}\right)\right] \propto \ln\left(\frac{t}{\tau}\right)^3 \tag{6}$$

The equation theoretically suggests a straight line in the plot with a slope of 1/S. Based on this, linear fittings are carried out, and the S values are calculated in Fig. 8b. The values are not well consistent with the typical values, i.e., 6, 8, and 10. This can be explained by the overwhelming migration effect (or diffusion effect) between Tb^{3+} [43,45,46], through which the radiationless energy is randomly distributed on the cations.

3.4. Magnetoluminescence

Along with the rapid development of high-density memory, photoelectronic devices and applications in high magnetic fields, researchers have paid great attention to the luminescence and electrical conductivity of materials exposed to an external magnetic field. In most papers, ML refers to PL or EL (electroluminescence) affected by the applied magnetic field [21]. This has been observed in some semiconductor nanostructures and organic compounds [22,23,28,47], typically under strong magnetic fields and/or low temperatures. In spite of the widely investigated PL and EL, little work has been done to fully understand the process of ML. So far, the mechanism of ML has been attributed to spin-dependent excitation processes, intercharge spin-spin interactions, and Lorentz effects [21].

Fig. 9a manifests the PL evolution for all samples affected by the applied magnetic field. Fig. 9b shows the relations of the integrated PL intensity to the magnetic field and the apparatus used for the ML measurement. All emission peak positions remain unchanged regardless of the applied magnetic field. No evident change in the PL intensity is noted for the pure TAG sample. However, a conspicuous fall in the PL intensity appears as the amount of Y rises when increasing the magnetic

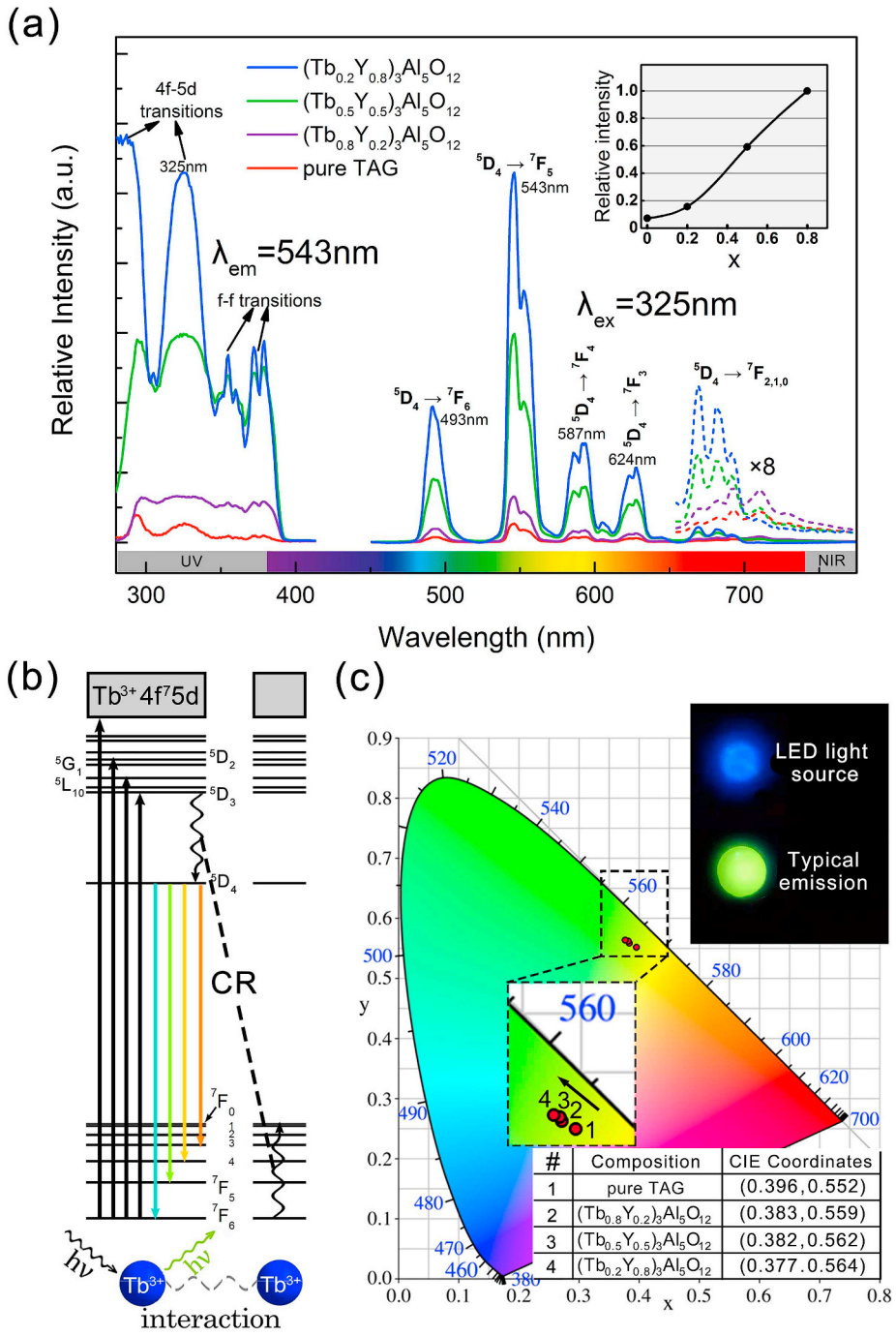

Fig. 7. (a) Excitation and PL spectra of $(Tb_{1-x}Y_x)_3Al_5O_{12}$ ceramics. Inset: integrated PL intensity of samples. (b) Energy level diagram of Tb^{3+} and the PL mechanism. (c) Color coordinates in CIE-1931 color space chromaticity diagram excited by a 365 nm LED source. Inset: a photo of a typical sample's PL. (For interpretation of the references to color in this figure legend, the reader is referred to the Web version of this article.)

field intensity. When the amount of Y reaches 80 mol.%, the emission intensity exhibits the greatest decline of approximately 45% under a 30 mT magnetic field, as demonstrated in Fig. 9b.

The result indicates that a higher concentration of Y leads to a more sensitive decline under the applied magnetic field, which is closely related to the evolution of the electronic energy levels of Tb^{3+} with the increase of Y content combined with the effect of a magnetic field. The crystal field and Zeeman effect may be the two main factors responsible for this phenomenon. Here, we only discuss the $^5D_4$ and ^7F_J energy levels of Tb^{3+}, since they are the main related electronic states of the luminescence. Observations and calculations have revealed that the energy gaps between upper and lower Stark sublevels of the $^5D_4$ and most of the ^7F_J multiplet in Tb^{3+}-doped YAG crystal are smaller than those in pure TAG crystal [48], indicating that the crystal field splitting of Tb^{3+} is weakened with the increasing substitution of Y^{3+} for Tb^{3+} and the sublevels get closer with each other. Furthermore, when exposed to a magnetic field, the Stark sublevels undergo a second splitting [24,49,50], which is referred to as the Zeeman effect, typically weakening the luminescence along with the increase of the magnetic field intensity. And it has been demonstrated that the magnetic field makes a difference to the intervals and ordering of the energy level fine structures, and neighboring sublevels may cross in some cases [24,49], therefore the radiative transition probabilities between these levels can be altered [49,51,52]. In addition, the Stark levels of initial (or final)

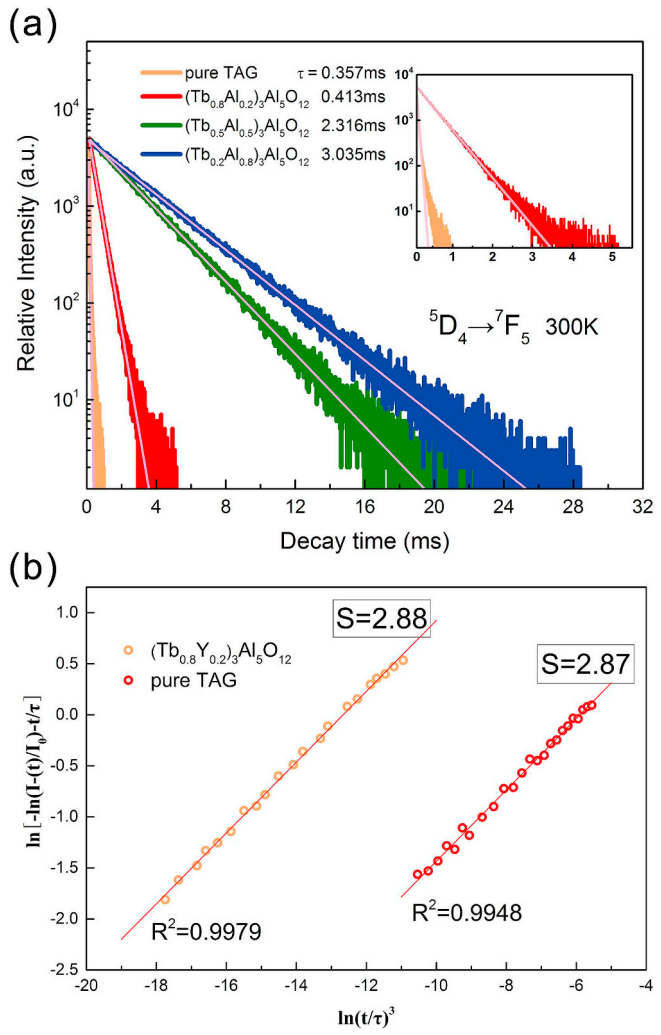

Fig. 8. (a) Decay curves, single exponential fittings and lifetimes of Tb^{3+} $^5D_4 \rightarrow {}^7F_5$ emission for $(Tb_{1-x}Y_x)_3Al_5O_{12}$ ceramics. Inset: enlarged image for pure TAG and $(Tb_{0.8}Y_{0.2})_3Al_5O_{12}$ samples. (b) A plot of the experimental data (scatter) from the time-resolved measurement of $^5D_4 \rightarrow {}^7F_5$ emissions and theoretical fittings (solid line), according to Eq. (6) (The values of R^2 stand for the quality of the fitting).

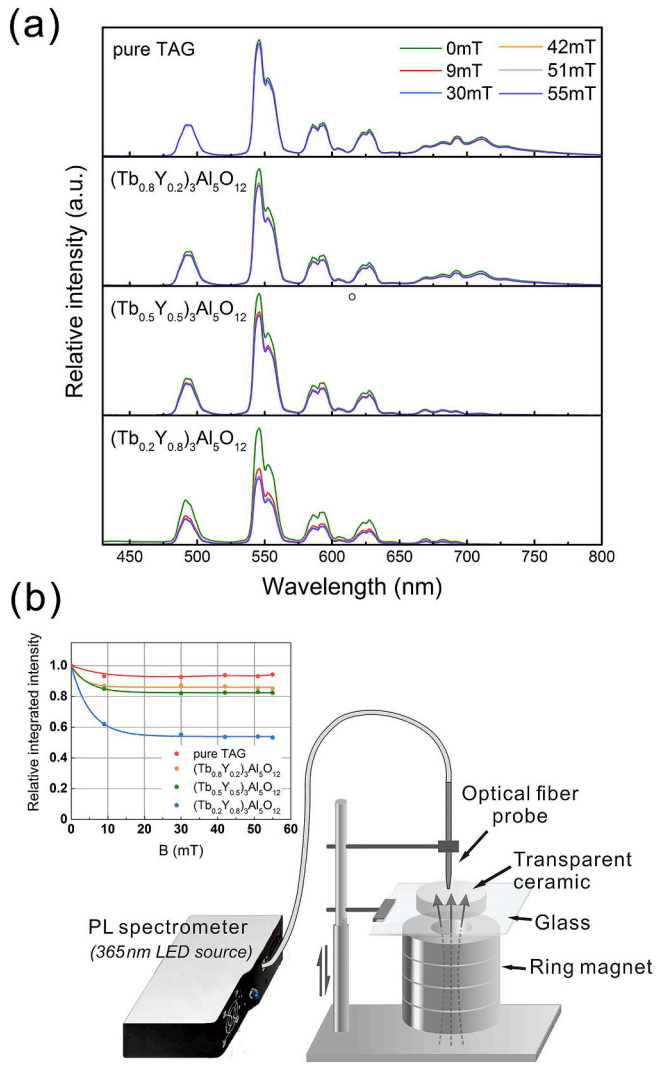

Fig. 9. (a) PL curves of the samples under different applied magnetic field. (b) Plots of relative integrated intensities of sample PL as a function of the intensity of the magnetic field, and the scheme for ML measurement.

states can be "mixed" under the magnetic field in the magneto-optically active transition process of Tb^{3+}, during which the energy splitting of the closely located Stark levels will be virtually inconspicuous [51]. U. V. Valiev et al. pointed that in the magnetic field this "mixing" effect of non-degenerate electronic states of Tb^{3+} plays a specific role in the radiative 4f-4f transitions, which can lead to the modulation of magneto-optical activity [52]. Specifically in this work, the introduction of Y narrows the gaps of Stark sublevels of Tb^{3+}, and this may be beneficial to the "mixing" effect of the adjacent levels under the magnetic field, leading to the greater decline of the luminescence.

It is quite noteworthy in this case that the ML of $(Tb_{1-x}Y_x)_3Al_5O_{12}$ emerges under room temperature and does not demand a strong magnetic field, which is rather meaningful for potential applications into photoelectronic devices with precise magnetic control, such as miniature optical probes and magnetic imaging.

4. Conclusions

We have successfully prepared $(Tb_{1-x}Y_x)_3Al_5O_{12}$ luminescent transparent ceramics. The Y-containing samples exhibit solid solution phases between TAG and YAG with fine crystallization, and the average grain size decreases as the Y content increases. The introduction of Y decreases the absorbance and increases the transmittance. The refractive index curve of the $(Tb_{1-x}Y_x)_3Al_5O_{12}$ sample evolves towards higher values near those of YAG as the Y content increases. With the introduction of Y, the PL intensity of the TAG can be enhanced by up to 14 times, and the RT lifetime of the $^5D_4 \rightarrow {}^7F_5$ emission is prolonged by up to 3.035 ms, showing efficient and long-lasting PL. The deviation from the single exponential decay behavior of the $^5D_4 \rightarrow {}^7F_5$ emission for $x = 0$ and 0.2 is caused by a radiationless process involving Tb^{3+} and impurities. The PL intensity declines more significantly for the samples with higher amounts of Y when the magnetic field intensity increases, which can be easily applied in photoelectronic devices and magnetism-controlled devices, such as optical probes, magnetic field detectors and controllable light sources. We believe that our work is helpful to further explore the multifunctional applications of TAG materials and hopefully sheds light on the magnetoluminescence research.

Declaration of competing interest

The authors declare that they have no known competing financial interests or personal relationships that could have appeared to influence the work reported in this paper.

Acknowledgements

This work was financially supported by the National Natural Science Foundation of China (NSFC) (11474104, 51672090). We would like to thank Prof. Bingjia Xu's group for support with the PL measurements.

References

[1] Y.R. Do, J.W. Bae, Application of photoluminescence phosphors to a phosphor-liquid crystal display, J. Appl. Phys. 88 (2000) 4660–4665.
[2] J. Yang, C. Zhang, C. Peng, C. Li, L. Wang, R. Chai, J. Lin, Controllable red, green, blue (RGB) and bright white upconversion luminescence of Lu_2O_3:Yb^{3+}/Er^{3+}/Tm^{3+} nanocrystals through single laser excitation at 980 nm, Chem. Eur J. 15 (2009) 4649–4655.
[3] K. Hanzawa, S. Iimura, H. Hiramatsu, H. Hosono, Material design of green-light-emitting semiconductors: perovskite-type sulfide $SrHfS_3$, J. Am. Chem. Soc. 141 (2019) 5343–5349.
[4] K. Li, H. Wang, X. Liu, W. Wang, Z. Fu, Mn^{2+} activated MgAlON transparent ceramic: a new green-emitting transparent ceramic phosphor for high-power white LED, J. Eur. Ceram. Soc. 37 (2017) 4229–4233.
[5] A. Ikesue, Y.L. Aung, Ceramic laser materials, Nat. Photonics 2 (2008) 721–727.
[6] L.J. Xu, C.Z. Sun, H. Xiao, Y. Wu, Z.N. Chen, Green-light-Emitting diodes based on tetrabromide manganese(II) complex through solution process, Adv. Mater. 29 (2017) 1605739.
[7] X. Zhang, H.-C. Wang, A.-C. Tang, S.-Y. Lin, H.-C. Tong, C.-Y. Chen, Y.-C. Lee, T.-L. Tsai, R.-S. Liu, Robust and stable narrow-band green emitter: an option for advanced wide-color-gamut backlight display, Chem. Mater. 28 (2016) 8493–8497.
[8] M.S. Alias, Z. Liu, A. Al-Atawi, T.K. Ng, T. Wu, B.S. Ooi, Continuous-wave optically pumped green perovskite vertical-cavity surface-emitter, Opt. Lett. 42 (2017) 3618–3621.
[9] S. Zhang, B. Zhu, S. Zhou, S. Xu, J. Qiu, Multi-photon absorption upconversion luminescence of a Tb^{3+}-doped glass excited by an infrared femtosecond laser, Opt. Express 15 (2007) 6883–6888.
[10] Y.L. Aung, A. Ikesue, Development of optical grade $(Tb_xY_{1-x})_3Al_5O_{12}$ ceramics as Faraday rotator material, J. Am. Ceram. Soc. 100 (2017) 4081–4087.
[11] J. Ding, W. Jin, Q. Chen, C. Hou, Y. Yu, L. Su, C. Li, F. Zeng, A. Wu, Optical properties, magnetooptical properties and terahertz time-domain spectrum of $Tb_3Sc_2Al_3O_{12}$ crystals grown by optical floating zone methods, Opt. Mater. Express 8 (2018) 2880–2886.
[12] J. Dai, Y. Pan, T. Xie, H. Kou, J. Li, Highly transparent $Tb_3Al_5O_{12}$ magneto-optical ceramics sintered from co-precipitated powders with sintering aids, Opt. Mater. 78 (2018) 370–374.
[13] J. Dai, Y. Pan, W. Wang, W. Luo, T. Xie, H. Kou, J. Li, Fabrication of $Tb_3Al_5O_{12}$ transparent ceramics using co-precipitated nanopowders, Opt. Mater. 73 (2017) 38–44.
[14] J. Dai, I.L. Snetkov, O.V. Palashov, Y. Pan, H. Kou, J. Li, Fabrication, microstructure and magneto-optical properties of $Tb_3Al_5O_{12}$ transparent ceramics, Opt. Mater. 62 (2016) 205–210.
[15] C. Chen, S. Zhou, H. Lin, Q. Yi, Fabrication and performance optimization of the magneto-optical $(Tb_{1-x}R_x)_3Al_5O_{12}$ (R = Y, Ce) transparent ceramics, Appl. Phys. Lett. 101 (2012) 131908–131911.
[16] H. Yin, Y. Gao, Y. Gong, R. Buchanan, J. Song, M. Li, Wavelength dependence of Tb^{3+} doped magneto-optical glass Verdet constant, Ceram. Int. 44 (2018) 10929–10933.
[17] Y. Zorenko, V. Gorbenko, T. Voznyak, M. Batentschuk, A. Osvet, A. Winnacker, Luminescence of Mn^{2+} ions in $Tb_3Al_5O_{12}$ garnet, J. Lumin. 130 (2010) 380–386.
[18] Q. Meng, Y. Liu, Y. Fu, Y. Zu, Z. Zhou, Synthesis and luminescent properties of $Tb_3Al_5O_{12}$:Ce^{3+} phosphors for warm white light emitting diodes, J. Mol. Struct. 1151 (2018) 112–116.
[19] D. Nakauchi, G. Okada, N. Kawano, N. Kawaguchi, T. Yanagida, Luminescent and scintillation properties of Ce-doped $Tb_3Al_5O_{12}$ crystal grown from Al-rich composition, Appl. Phys. Express 10 (2017) 072601.
[20] Y. Zorenko, V. Gorbenko, T. Voznyak, T. Zorenko, B. Kuklinski, R. Turos-Matysyak, M. Grinberg, Luminescence properties of phosphors based on $Tb_3Al_5O_{12}$ (TbAG) terbium-aluminum garnet, Opt Spectrosc. 106 (2009) 365–374.
[21] M.C. Wong, L. Chen, M.K. Tsang, Y. Zhang, J. Hao, Magnetic-Induced luminescence from flexible composite laminates by coupling magnetic field to piezophotonic effect, Adv. Mater. 27 (2015) 4488–4495.
[22] T. Duc Nguyen, Y. Sheng, J.E. Rybicki, M. Wohlgenannt, Magnetoconductivity and magnetoluminescence studies in bipolar and almost hole-only sandwich devices made from films of a π-conjugated molecule, Sci. Technol. Adv. Mater. 9 (2016) 024206.
[23] S. Kimura, T. Kusamoto, S. Kimura, K. Kato, Y. Teki, H. Nishihara, Magnetoluminescence in a photostable, brightly luminescent organic radical in a rigid environment, Angew. Chem. Int. Ed. 57 (2018) 12711–12715.
[24] L.F. Chibotaru, V.K. Tikhomirov, D. Saurel, V.V. Moshchalkov, Extraordinary magnetic field induced suppression of luminescence in Er^{3+}-doped nano-glass-ceramics, J. Appl. Phys. 106 (2009) 053502.
[25] V.I. Belotelov, I.A. Akimov, M. Pohl, V.A. Kotov, S. Kasture, A.S. Vengurlekar, A.V. Gopal, D.R. Yakovlev, A.K. Zvezdin, M. Bayer, Enhanced magneto-optical effects in magnetoplasmonic crystals, Nat. Nanotechnol. 6 (2011) 370–376.
[26] W. Wernsdorfer, Quantum dynamics in molecular nanomagnets, C. R. Chim. 11 (2008) 1086–1109.
[27] Q. Ju, D. Tu, Y. Liu, R. Li, H. Zhu, J. Chen, Z. Chen, M. Huang, X. Chen, Amine-functionalized lanthanide-doped $KGdF_4$ nanocrystals as potential optical/magnetic multimodal bioprobes, J. Am. Chem. Soc. 134 (2012) 1323–1330.
[28] G. Dai, Z. Zhong, X. Wu, S. Zhan, S. Hu, P. Hu, J. Hu, S. Wu, J. Han, Y. Liu, Magnetic tuning of upconversion luminescence in Au/$NaGdF_4$:Yb^{3+}/Er^{3+} nanocomposite, Nanotechnology 28 (2017) 155702.
[29] V.K. Tikhomirov, L.F. Chibotaru, D. Saurel, P. Gredin, M. Mortier, V.V. Moshchalkov, Er^{3+}-doped nanoparticles for optical detection of magnetic field, Nano Lett. 9 (2009) 721–724.
[30] P. Duan, P. Liu, X. Xu, W. Wang, Z. Wan, S. Zhang, Y. Wang, J. Zhang, Fabrication of transparent $Tb_3Al_5O_{12}$ ceramics by hot isostatic pressing sintering, J. Am. Ceram. Soc. 100 (2017) 2893–2900.
[31] P. Duan, P. Liu, X. Xu, W. Wang, Z. Wan, S. Zhang, Y. Wang, J. Zhang, Fabrication and properties of $(Tb_xY_{1-x})_3Al_5O_{12}$ transparent ceramics by hot isostatic pressing, Opt. Mater. 72 (2017) 58–62.
[32] K. Richter, R. Wannemacher, J. Heber, D. Mateika, Direct observation of migration of optical excitation energy in YAG:Tb^{3+}, J. Lumin. 47 (1990) 169–175.
[33] J. Bodzenta, A. Kaźmierczak-Bałata, K. Wokulska, J. Kucytowski, P. Szperlich, T. Łukasiewicz, B. Hofman, Analysis of influence of Yb concentration on thermal, elastic, optical and lattice parameters in YAG single crystal, J. Alloy. Comp. 473 (2009) 245–249.
[34] C. Hu, Y. Shi, X. Feng, Y. Pan, YAG:Ce/(Gd,Y)AG:Ce dual-layered composite structure ceramic phosphors designed for bright white light-emitting diodes with various CCT, Opt. Express 23 (2015) 18243–18255.
[35] E.D. Palik, Handbook of Optical Constants of Solids, first ed., Elsevier Science, UK, 1998.
[36] S. Ding, H. Zhang, R. Dou, W. Liu, D. Sun, Q. Zhang, Theoretical and experimental studies of electronic, optical and luminescent properties for Tb-based garnet materials, J. Solid State Chem. 263 (2018) 123–130.
[37] H. Kimura, A. Miyazaki, Lattice parameter dependence of refractive index and dielectric constant of czochralski grown rare-earth garnet single crystals in solid solution, Jpn. J. Appl. Phys. 41 (2002) 5334–5335.
[38] Y. Onishi, T. Nakamura, S. Adachi, Luminescence properties of $Tb_3Al_5O_{12}$ garnet and related compounds synthesized by the metal organic decomposition method, J. Lumin. 183 (2017) 193–200.
[39] Y. Tosaka, S. Adachi, Photoluminescence properties and energy-level diagrams in (Ce^{3+}, Tb^{3+})-codoped KCl green phosphor, J. Lumin. 156 (2014) 157–163.
[40] N. Bodenschatz, R. Wannemacher, J. Heber, D. Mateika, Electronically resonant optical cross relaxation in YAG:Tb^{3+}, J. Lumin. 47 (1990) 159–167.
[41] W.F. van der Weg, T.J.A. Popma, A.T. Vink, Concentration dependence of UV and electron-excited Tb^{3+} luminescence in $Y_3Al_5O_{12}$, J. Appl. Phys. 57 (1985) 5450–5456.
[42] J.R. Lakowicz, Principles of Fluorescence Spectroscopy, third ed., Springer, US, 2006.
[43] K.-S. Sohn, Y.Y. Choi, H.D. Park, Photoluminescence behavior of Tb^{3+}-activated YBO_3 phosphors, J. Electrochem. Soc. 147 (2000) 1988–1992.
[44] M. Inokuti, F. Hirayama, Influence of energy transfer by the exchange mechanism on donor luminescence, J. Chem. Phys. 43 (1965) 1978–1989.
[45] J.P. van der Ziel, L. Kopf, L.G. Van Uitert, Quenching of Tb^{3+} luminescence by direct transfer and migration in aluminum garnets, Phys. Rev. B 6 (1972) 615–623.
[46] M. Yokota, O. Tanimoto, Effects of diffusion on energy transfer by resonance, J. Phys. Soc. Jpn. 22 (1967) 779–784.
[47] M.H. Jeon, K.H. Yoo, M.G. Sung, I.T. Jeong, J.C. Woo, L.R. Ram-Mohan, A magnetoluminescence study of quantum wells in an inplane magnetic field, Solid State Commun. 150 (2010) 1782–1784.
[48] J.B. Gruber, B. Zandi, U.V. Valiev, S.A. Rakhimov, Crystal-field splitting of some quintet states of Tb^{3+} in aluminum garnets, Phys. Rev. B 69 (2004) 115103.
[49] J. Zhang, Z. Zhong, X. Wang, Z. Ma, S. Wang, Y. Han, J. Han, Large photoluminescence enhancement of Er^{3+}: $GdVO_4$ crystal in both green and middle infrared regions under moderate low magnetic fields, Opt. Mater. Express 6 (2016) 3446–3454.
[50] U.V. Valiev, V. Nekvasil, S.I. Mukhamedhanova, D.R. Dzhuraev, K.S. Saidov, Experimental definition of zeeman splitting of excited states of Tb^{3+} ion in $Y_3Al_5O_{12}$, Phys. Status Solidi B 213 (1999) 493–501.
[51] U.V. Valiev, J.B. Gruber, I.A. Ivanov, G.W. Burdick, H. Liang, L. Zhou, D. Fu, O.V. Pelenovich, V.O. Pelenovich, Z. Lin, Magnetooptics of the luminescent transitions in Tb^{3+}:$Gd_3Ga_5O_{12}$, Opt. Mater. 46 (2015) 282–291.
[52] U.V. Valiev, U.R. Rustamov, B.Y. Sokolov, V. Nekvasil, R.A. Rupp, M. Fally, I. Amin, Features of circularly polarized luminescence of the paramagnetic garnets $Y_3Al_5O_{12}$:Tb^{3+} and $Y_3Al_5O_{12}$:Ho^{3+} in magnetic field, Phys. Status Solidi B 231 (2002) 98–105.